Short-Term Forecasting of High Resolution Local DNI Maps with Multiple Fish-Eye Cameras in Stereoscopic Mode

Philippe Blanc[1,a)], Pierre Massip[1], Andreas Kazantzidis[2], Panagiotis Tzoumanikas[2], Pascal Kuhn[3], Stefan Wilbert[3], David Schüler[3], Christoph Prahl[3]

[1]*MINES ParisTech, PSL Research University, O. I. E. – Centre Observation, Impacts, Energy, CS 10207, F-06904, Sophia Antipolis CEDEX, France.*
[2]*Laboratory of Atmospheric Physics, Physics Department, University of Patras, 26500, Patras, Greece*
[3]*German Aerospace Center (DLR), Institute of Solar Research, Plataforma de Almería, Ctra. de Senés s/n km 4, 04200 Tabernas, Spain.*

a) Corresponding author: philippe.blanc@mines-paristech.fr

Abstract. Nowcasting of high resolution maps of direct normal irradiance (DNI) is of interest to efficiently operate Concentrated Solar Power plants. The paper presents a state-of-the-art and innovative methodology, developed in the framework of the FP7 DNICast project, to derive nowcasting of DNI maps from fish-eye cameras in stereoscopic mode. This methodology has been applied at the *Plataforma Solar de Almeria*: fish-eye cameras at distances from each other between 500 m and 900 m have been used in stereoscopic mode to produce nowcasted 1-min time series of decametric DNI maps.

INTRODUCTION

Real-time and very short-term forecasting up to 15 min to 30 min updated every minute –named hereinafter nowcasting– of high resolution maps of direct normal irradiance (DNI) may be used to efficiently operate Concentrated Solar Power (CSP) plants. For example, such nowcasting of spatially resolved DNI over a CSP plant enables a better management of the flow rate of the working fluid or the defocusing mirrors.

Having these nowcasted DNI maps both in high spatial resolution –decametric– and high temporal resolution – 1 min or less– is a challenging task that cannot be accurately achieved by satellite products or numerical weather predictions due to their limited spatial and temporal resolutions. The use of ground-based fish-eye cameras providing time series of hemispherical images of the sky has been emerging in scientific community of solar energy in order to capture the high spatial and temporal variability of clouds and provide the needed inputs for solar nowcasting [1-4].

This paper presents a state-of-the-art methodology used to derive the parameters needed for the nowcasting of DNI maps making use of fish-eye cameras in stereoscopic mode. The proposed methodology was developed in the framework of the DNICast project [5]. At the *Plataforma Solar de Almeria* (PSA), a dependency of the *Centro de Investigaciones Energéticas, Medioambientales y Tecnológicas* (CIEMAT), four fish-eye cameras have been setup by the *Deutsches Zentrum für Luft- und Raumfahrt* (DLR, German Aerospace). The distances between these cameras are ranging from 500 m to 900 m from each other, as depicted in Fig. 1. Time series of hemispherical images from these cameras have been used in stereoscopic mode to produce nowcasted 1-min DNI maps over a 30 km x 30 km region with a spatial resolution up to 10 m.

The objective of this paper is to present and illustrate the proposed methodology. The validation of these nowcasted DNI maps with a specific network of radiometers and shadow cameras –cameras filming the ground from the top– over more than 6 months from 2014 and 2015 is presented separately in another communication [6].

FIGURE 1. Locations of the four fish-eye cameras installed by the DLR at the *Plataforma Solar de Almeria* (PSA) in framework of the DNICast Project.

METHODOLOGY FOR THE DNI MAPS NOWCASTING

To sum up, the methodology for the nowcasting of DNI maps is as follows: At each time frame, the hemispherical image of one camera is analyzed to detect clouds. The previous image from the same camera is used to assess the apparent cloud motion vectors (CMV). With a second –or more– fish-eye camera(s) at different geographic location(s), it is possible to determine the position and the cloud base height (CBH) of the detected clouds and therefore to provide 3D map of clouds over a radius of approximately 15 km in real-time using adapted stereoscopic techniques. Knowing the 3D positions of the clouds and the apparent cloud displacement between two consecutive images, positions and velocities of cloud shadows can be nowcasted, thus enabling spatially resolved DNI nowcasting.

The purpose of this section is to describe the different steps of the methodology in detail.

Preliminary Step: the Setup and the Geometric Calibration of the Fish-eye Cameras

The fish-eye cameras installed by the DLR at the PSA are commercial security cameras (MOBOTIX Q24) that are relatively cheap, easy to setup and robust. These cameras have been setup to provide hemispherical images of effective size of 2.4 Mpixels with a sampling period of 30 s. The corresponding angular resolution of the hemispherical sky images is approximately 0.1°.

The geometric calibration of each fish-eye cameras involved are very important, namely for the 3D reconstruction in stereoscopic mode. This calibration, comprising two steps, is described by [7]. The first step is the intrinsic calibration to determine the internal parameters of the camera (center of the focal plane, optical distortions, etc.). This calibration is done by acquiring several images of a checkerboard pattern (Fig. 2a) under different positions and makes use of the Matlab toolbox OcamCalib [8]. The second step is the extrinsic calibration. It consists in the determination of the 3D orientation of the camera and is done by comparing the theoretical angular positions of the Sun computed with Solar Geometry 2 [9] and its center detected in the sky images acquired during various clear-sky days (Fig. 2b). After this optimization, the RMSE of the angular position of the detected sun positions compared to the theoretical ones is ranging between 0.14 and 0.45°, both in azimuth and elevation.

The geometric calibration done for each camera provides:
- The direct localization function providing the line of sight (LoS) for a given pixel ;
- Inverse localization function determining the pixel corresponding to a given 3D point in the world.

(a)   (b)
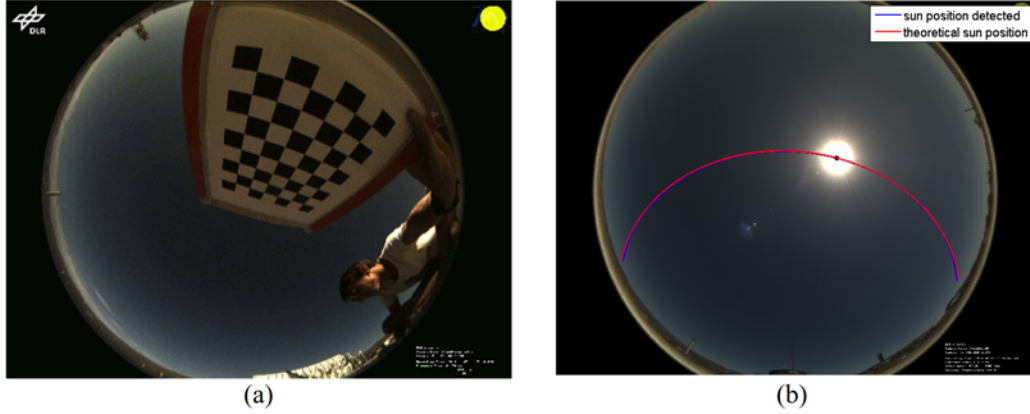
FIGURE 2. Example for the geometric calibration of a fish-eye camera, using a checkerboard pattern (a) for the intrinsic calibration and (b) the comparison of the theoretical sun positions with the one detected in sky images under clear-sky condition.

The Cloud Detection and Classification

The method for the detection of clouds –and the estimation of total cloud coverage– is based on multi-color criteria using the red, green and blue intensities of the sky images [5]. According to validations done under a variety of cloud conditions and solar zenith angles, 83 % and 94 % of the total cloud cover estimated on images agree with the corresponding visual meteorological observations to within respectively 1 and 2 *octas* [10].

(a)   (b)
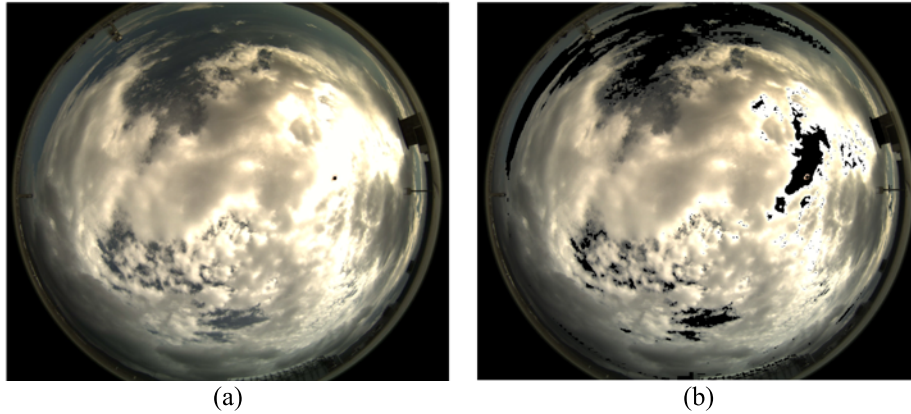
FIGURE 3. Example of cloud/clear sky segmentation with cumulus clouds. (a) Original sky image. (b) Clear-sky pixels are represented in black.

Classification algorithms based on color and textural features were used for the classification into different cloud types. According to results, the accuracy of the classifier ranges between 80 and 95 %.

Estimation of the Cloud Base Height (CBH)

Once pixels of clouds have been detected in one sky image (image A), the objective is to assess their corresponding CBH using a second sky image (image B), acquired at the same time from a distant fish-eye camera, using techniques of stereoscopic photogrammetry to assess CBH from the observed parallaxes.

More precisely, cloudy pixels with significant textural and contrast information in their vicinity are selected in the image A as potential tie points (TPs). The level of significant textural and contrast information is locally

assessed with the L2-norm of the gradient of the image A. In order to have, as far as possible, a homogeneous distribution of these potential TPs, the selection is done within a predefined 32x32 grid applied on the cloud mask. On each grid element, local maxima of the L2-norm of the gradient are detected and the pixels corresponding to their five greatest values are selected, provided they are above a global threshold.

The matching of each potential TPs in the image B is done by maximizing the normalized correlation coefficient (NCC) between 10x10 context windows within a search area. To improve this matching procedure, the image B is first resampled in the geometry of the image A with a given arbitrary constant CBH (4500 m). The local search area is then locally defined assuming possible CBH ranging between 1000 m and 10000 m. This matching procedure is considered as successful if the maximum NCC is greater than 0.8 and, finally, if the minimum distance of the corresponding LoS is lower than 50 m.

Due to local saturations or, on contrary, local low luminance, pixels for which the CBH have been successfully assessed are generally sparse and localized on the boundary of the clouds. In order to filter errors in altitude estimation, a KNN classifier is applied to this set of scattered CBH estimations to automatically detect up to five different CBH layers. A nearest neighbor scattered interpolation technique is then used to assess the CBH for each cloudy pixel in image A. As a result, each cloudy pixel is related to a 3D position.

Compared to CBH provided by the ceilometer installed at the PSA next to camera 1 (see Fig. 1), the RMSE is between 500 and 800 m depending on the cloud conditions, with a correlation coefficient greater than 0.85. Figure 4 proposes as an example, for the day 2014/05/24, the scatterogram and the statistical comparison between CBH measured by the ceilometer and the estimated ones with the fish-eye cameras at the very vertical of the ceilometer.
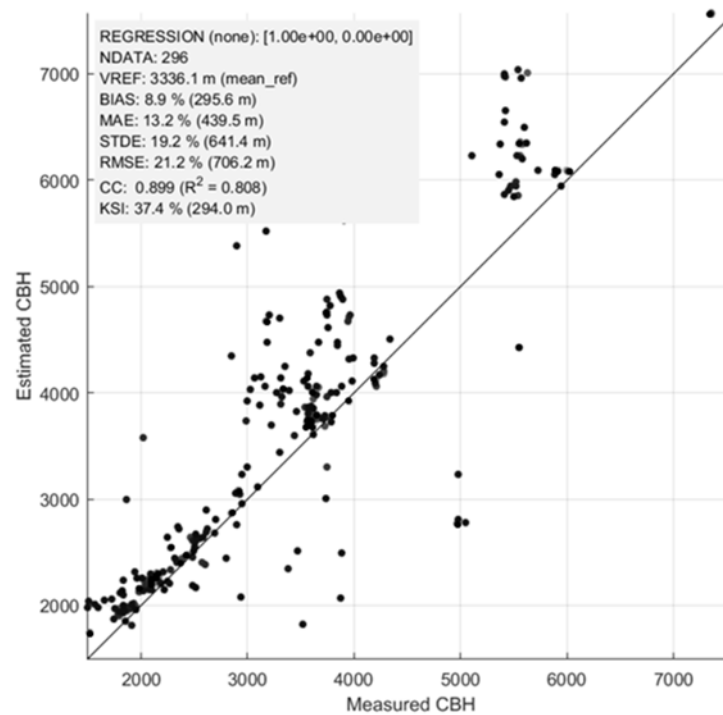

FIGURE 4. Example for the day 2014/05/24 of the scatterogram and the statistical comparison between CBH measured by the ceilometer installed at the PSA and estimated concomitant CBH with the fish-eye cameras HP and KONTAS (see Fig. 1) at the very vertical of the ceilometer.

Estimation of the Cloud Motion Vectors (CMV) per Class of Altitude

The same approach based on NCC is used for the estimation of the CMV. Starting from the set of pixels in image A that has been successfully matched for the CBH step, the matching procedure is applied again but searching in the previous image A, 30 s before. For each TP, the matching is considered as successful if the maximum NCC is greater than 0.8, giving a local estimation of the apparent CMV in the "pixel" geometry of the image A. Thanks to the corresponding estimated CBH and assuming no significant CMV vertical component, the apparent CMV is

transformed into a 3D CMV associated to each TP in image A. These CMV estimates for different CBH layers are then averaged per class of altitude among four classes: low (< 2500 m), medium-low (2500 m – 5000 m), medium-high (5000 m – 7500 m) and high altitudes (> 7500 m). Figure 5 shows an example of the CBH and CMV estimations. These averaged CMV estimates can be seen as estimates of North-South and East-West wind speeds for these four classes of altitude.
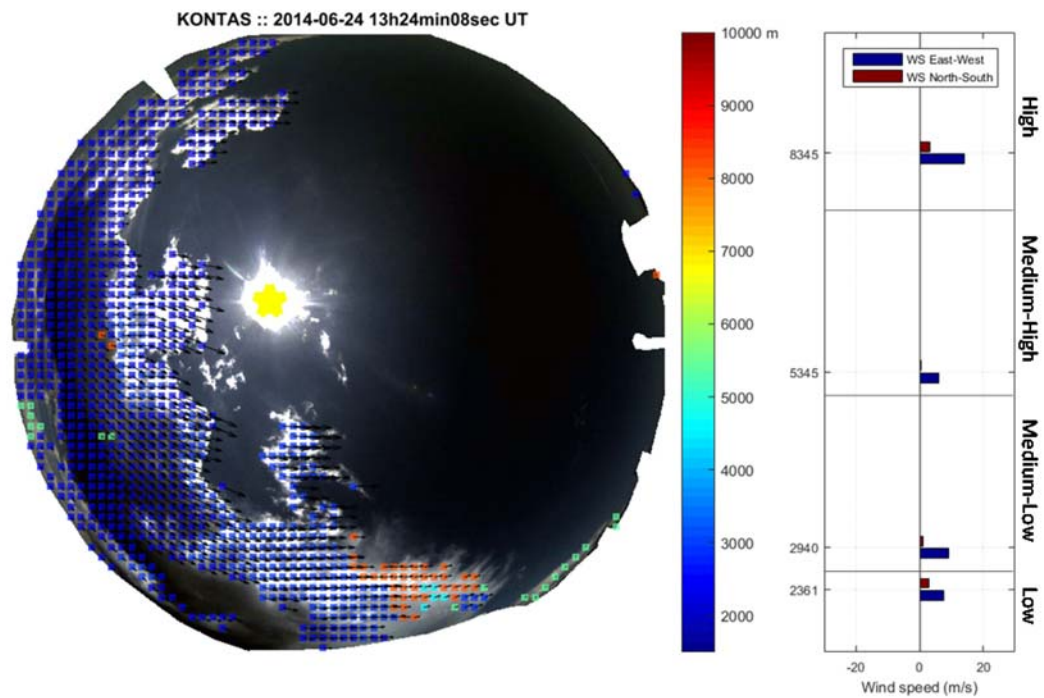
FIGURE 5. Example of a sky image with superimposed retrieved information of CBH (color patches) and CMV (velocity vectors in black).

Nowcasting of the Cloud Shadow on the Ground and the DNI
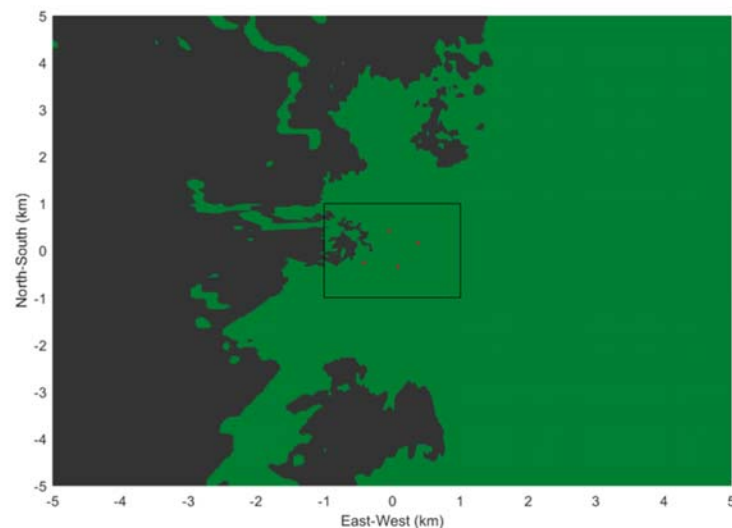
FIGURE 6. Example of nowcasted (t+5 min) cloud shadow (red dots represent the ASIs, dark areas are shaded), corresponding to Fig. 5.

Knowing the 3D positions of the detected clouds, assuming the persistence of the estimated CMV per class of altitude and considering only cloud advections, it is possible to forecast their future 3D positions along with their projected shadows on the ground (Fig. 6).

The transposition of these forecasted cloud shadows on the ground and the corresponding DNI values is not straightforward. Following [11], we have considered the decoupling in the DNI between:

- The DNI under clear sky condition (no clouds in the sky vault).
- The beam clear-sky index Kc only depending on the clouds characteristics (for the beam component).

The DNI under clear-sky condition is provided as a day-ahead forecast by the clear-sky irradiance model McClear [12]. The beam clear-sky index Kc should be related to the cloud shadow on the ground. Following the approach proposed by [4], historical beam clear-sky indexes measured in real-time by a pyrheliometer for the past 30 min is used. More precisely, median values of these "sliding window" historical beam clear-sky indexes is computed per classes of shadow clouds mixing the cloud segmentation and classification (section 2.2) and the CBH layers (section 2.3). These median values of Kc are then used to relate, for each pixel of the cloud shadow its corresponding estimated beam clear-sky index.

Figure 7 presents the 1-min DNI estimated for the place METAS (see Fig. 1) in real time –nowcasting with a null time horizon– obtained with the fish-eye cameras at the places HP and KONTAS, using the pyrheliometer located at the place HP. The correlation between the estimated DNI and the reference is greater than 0.94.
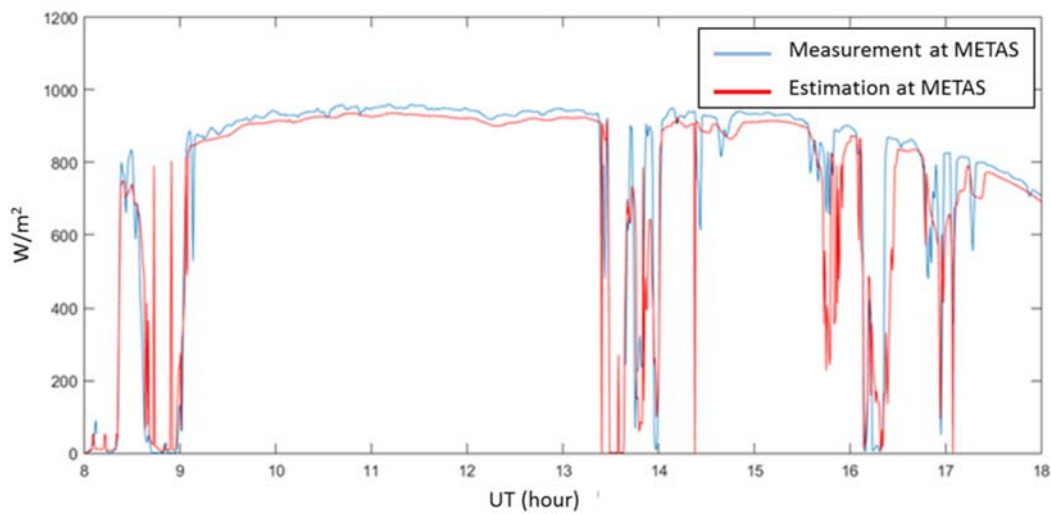
FIGURE 7. Example of real-time estimate of DNI (in red) for the day 2014/06/24 using fish-eye cameras HP and KONTAS compared to the reference one (in blue) provided by a pyrheliometer at the METAS station (see Fig. 1).

Figure 8a presents the 1-min DNI nowcasted with a time horizon of 15 min at METAS (see Fig. 1). As a comparison, Fig. 8c presents the corresponding nowcasted 1-min DNI obtained with a clear-sky index based persistence forecast for which one can notice the inherent systematic time-lag of 15 min in case of DNI variability induced by clouds. One can notice that the nowcasted DNI with the fish-eye cameras does not present this systematic time-lag of 15 min. Large ramps such the positive ones at 9h UT or at 14h UT or the negative ones at 13h20 UT or 16h20 UT are forecasted (partially for the latter). Nevertheless, some ramps are missing such as the ones around 8h30 UT and some nowcasted ramps are falsely detected such as the ones at 9h30 UT and 14h20 UT. In many situations, the nowcasted DNI presents very short term spikes, mainly due cloud false detection or cloud occlusions. Indeed, in case of multiple layers of clouds, upper clouds may be occulted by lower clouds, thus possibly creating "holes" in the cloud shadows. The correlation between the nowcasted DNI with the fish-eye cameras and the reference is 0.65, slightly better than the one obtained by the persistence method (0.64). When applying a 5-min causal median filter as a post-processing of the nowcasted DNI, the correlation coefficient increases to 0.76, filtering out the short-term DNI spikes but also introducing time-lag of few minutes (Fig 8b).

CONCLUSION AND PERSPECTIVES

The paper presents the methodology used to produce, in real-time, nowcasted 1-min decametric DNI maps over a region of interest up typically to 30 km x 30 km, using fish-eye cameras in stereoscopic mode. The process takes less than 30 s and can be envisaged to be applied in real-time., Notably it comprises:

- Cloud detection and classification of sky images provided by one of the fish-camera.
- CBH estimation based on normalized cross-correlation matching process using, in addition, sky images provided by another distant fish-eye camera, in stereoscopic mode.
- CMV estimation per class of altitude based on normalized cross-correlation matching process using two consecutive sky images from the same fish-eye camera, with 30 s of time-lag.
- Nowcast of cloud shadow maps on the ground and transposition into DNI maps.

In-depth analysis of the nowcasting results will be presented in another communication [9]. The results of the nowcasting are far from being perfect but are encouraging.

(a)

(b)
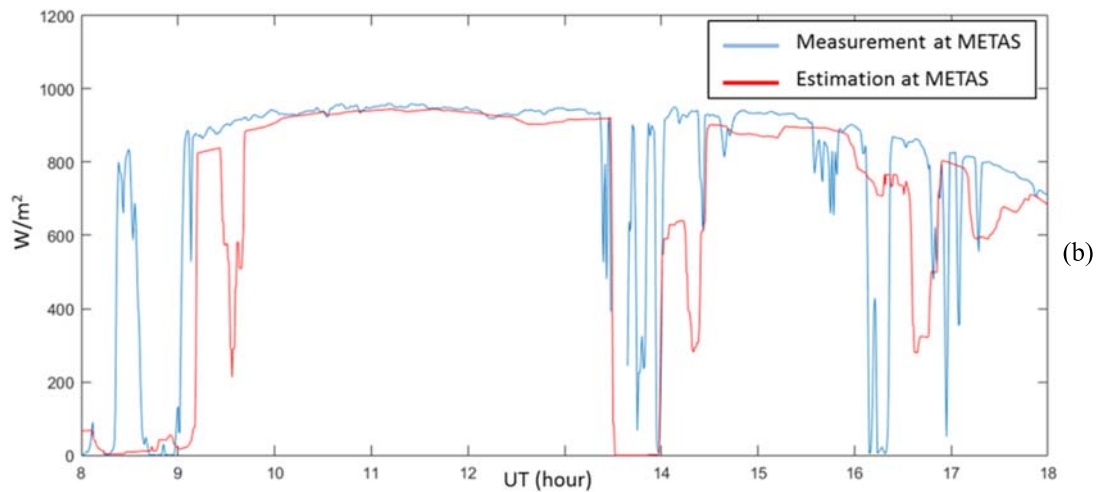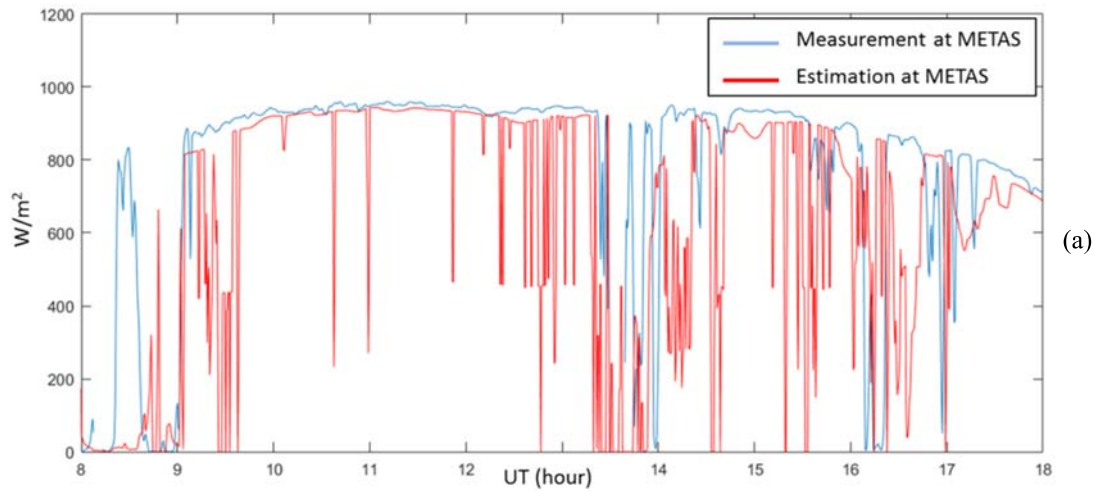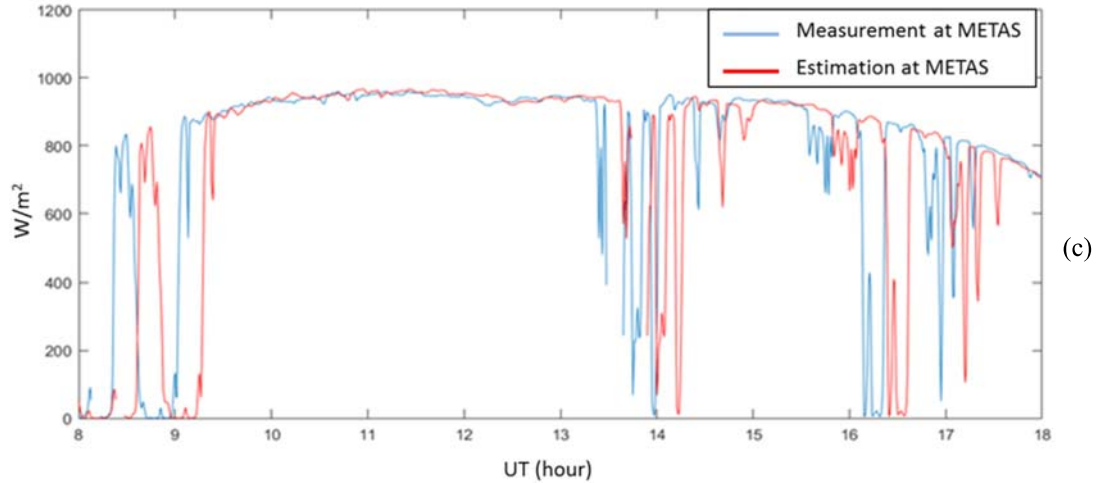
FIGURE 8. (a) Example of nowcasting (time horizon of 15 min) of DNI (in red) for the day 2014/06/24 using fish-eye cameras HP and KONTAS compared to the reference one (in blue) provided by a pyrheliometer at the METAS station (see Fig. 1). (b) Results of the post-processing with a 5-min causal median-filter on the nowcasted DNI (a) (c) Corresponding nowcasting of DNI using the clear-sky index persistence.

We have identified some key points explaining the difficulties and the complexity to obtain accurate nowcasts of DNI maps:

- The quality of the cloud detection is crucial for the whole chain of processing. Even if the cloud detection algorithm is efficient, the quality of the sky images as input is of very first importance, in particular in the circumsolar region: saturations, flares and halos create artifacts in the cloud detection and eventually in the nowcasted DNI maps.
- The localization of cloud shadows on the ground is very sensitive to errors in CBH estimation due to residual error in the geometric calibration –notably for low pixel elevation angles– or errors in the matching procedure. This sensitivity is all the more important that the sun elevation is low.
- The cloud occlusion in case of multiple layers of cloud possibly inducing "holes" in the cloud masks for the upper layers.
- The extreme complexity of the dynamic of the cloud cover, notably at these high spatial and temporal resolutions: the assumption of simple cloud advection with persistence of CMV is not always applicable.

As an intermediate result, this study has shown, that two fish-eye cameras in stereoscopic mode may provide, in real-time every 30 s, an overview of the cloud cover over a zone of interest of approximately 30 km x 30 km. This overview corresponds to a decametric cloud mask with retrieved CBH and CMV per class of altitude. Without going all the way to the nowcasting of DNI maps, this intermediate result may have, on its own, as a cheapest alternative to ceilometers– an interest for the efficient management of a large scale CSP plant but also in other applications for which high spatial and temporal resolution cloud cover information is important (e.g. airport management).

ACKNOWLEDGMENT

REFERENCES

1. D. Bernecker, C. Riess, E. Angelopoulou and J. Hornegger, "Continuous short-term irradiance forecasts using sky images," *Solar Energy*, **110**, 303–315 (2014).

2. Y. Chu, M. Li, H.T.C. Pedro and C.F.M. Coimbra, "Real-time prediction intervals for intra-hour DNI forecasts," *Renewable Energy*, **83**, 234-244 (2015).
3. Chauvin, R. 2016. "Évaluation de La Ressource Solaire Pour La Gestion Optimisée de Centrales CSP," Ph.D. thesis, Université de Perpignan Via Domitia, 2016.
4. T. Schmidt, J. Kalisch, E. Lorenz and D. Heinemann. "Evaluating the Spatio-Temporal Performance of Sky Imager Based Solar Irradiance Analysis and Forecasts," *Atmospheric Chemistry and Physics*, 16, 3399-3412, doi:10.5194/acp-16-3399-2016 (2016).
5. P. Massip, Ph. Blanc, A. Kazantzidis, P. Tzoumanikas. "DNICast: Report on algorithms for nowcasting methods based on sky imagers," Report D3.1., DNICast project, 29 pp, http://www.dnicast-project.net (2015).
6. P. Kuhn, S. Wilbert, D. Schüler, C. Prahl, T. Haase, L. Ramirez, L. Zarzalejo, A. Meyer, L. Vuilleumier, P. Blanc, J. Dubrana, M. Schroedter-Homscheidt, T. Hirsch and R. Pitz-Paal, "Validation of Spatially Resolved All Sky Imager Derived DNI Nowcasts," Abstract accepted in SolarPACES conference (2016).
7. C. Gauchet, P. Blanc, B. Espinar, B. Charbonnier and D. Demengel. "Surface Solar Irradiance Estimation with Low-Cost Fish-Eye Camera," in COST WIRE Workshop on Remote Sensing Measurements for Renewable Energy, 4 pp (2012).
8. D. Scaramuzza, A. Martinelli and R. Siegwart, "A toolbox for easily calibrating omnidirectional cameras," in Proc. 2006 IEEE/RSJ International Conference on Intelligent Robots and Systems, pp. 5695- 5701 (2006).
9. P. Blanc and L. Wald, "The SG2 Algorithm for a Fast and Accurate Computation of the Position of the Sun for Multi-Decadal Time Period," *Solar Energy*, **86**(10), 3072–3083, doi:10.1016/j.solener.2012.07.018 (2012).
10. A. Kazantzidis, P. Tzoumanikas, A.F. Bais, S. Fotopoulos and G. Economou, "Cloud detection and classification with the use of whole-sky ground-based images," *Atmospheric Research*, **113**, 80-88 (2012).
11. A. Oumbe, Z. Qu, P. Blanc, M. Lefèvre, L. Wald, and S. Cros, "Decoupling the Effects of Clear Atmosphere and Clouds to Simplify Calculations of the Broadband Solar Irradiance at Ground Level," *Geoscientific Model Development*, **7**, 1661–69, doi:10.5194/gmdd-7-2007-2014 (2014).
12. M. Lefèvre, A. Oumbe, P. Blanc, B. Espinar, B. Gschwind, Z. Qu, L. Wald, M. Schroedter-Homscheidt, C. Hoyer-Klick, A. Arola, A. Benedetti, J.W. Kaiser and J.-J. Morcrette, "McClear: A New Model Estimating Downwelling Solar Radiation at Ground Level in Clear-Sky Conditions," *Atmospheric Measurement Techniques*, **6**, 2403–18, doi:10.5194/amt-6-2403-2013 (2013).